Supplement of Atmos. Chem. Phys., 25, 8701–8718, 2025
https://doi.org/10.5194/acp-25-8701-2025-supplement

Atmospheric Chemistry and Physics
Open Access
EGU

Supplement of

Impacts of wildfire smoke aerosols on near-surface ozone photochemistry

Jiaqi Shen et al.

Correspondence to: Xiaomeng Jin (xiaomeng.jin@rutgers.edu)

Text S1. The 2020 wildfire season in California

Initiated by an unusual dry lightning siege on August 16–17, the season began with rapid growth and merging of numerous wildfire complexes (Lassman et al., 2023). Notable among these included the August Complex in the Coast Range of Northern California, the SCU Lightning Complex and the LNU Lightning Complex near the San Francisco Bay area, as well as the North Complex in Plumas and Butte counties. This initial phase was followed by a series of megafires in early September, culminating when the August Complex merged on September 9 to form the largest single wildfire in California's recorded history (CAL FIRE, 2020). Concurrently, a dry northeast wind event on September 8–9 drastically accelerated the spread of the North Complex towards the southwest, marking it as the most destructive wildfire of the season (CAL FIRE, 2020). Simultaneously, the Creek fire in the Sierras reached its peak intensity (Carreras-Sospedra et al., 2024). Moreover, Northern California was affected by smoke transported from Portland, Oregon around mid-September (Carreras-Sospedra et al., 2024; Lassman et al., 2023).

Throughout the 2020 California fire season, fires released approximately 1 million Mg of fine particulate matter ($PM_{2.5}$), exposing over half population to unhealthy air quality for a month or longer (Safford et al., 2022). Additionally, NO_x emissions from wildfires eroded the anthropogenic NO_x emissions reductions achieved during the COVID-19 lockdown, leading to higher statewide annual average NO_2 levels (Jin et al., 2023).

Table S1. HO_2 uptake coefficient (γ_{HO_2}) measured in previous laboratory and field studies.

Study	Temperature (K)	Relative humidity (%)	Aerosol type	γ_{HO_2}	Notes
(Taketani et al., 2010)	296 ± 2	20–92	levoglucosan particles;	<0.01–0.13	lab
			polystyrene latex particles	0.01–0.03	
(Lakey et al., 2015)	293 ± 2	32–80	glutaric acid, glyoxal, malonic acid, stearic acid, oleic acid, squalene, monoethanol amine sulfate, monomethyl amine sulfate	<0.004–0.008	lab
		32–76	humic acid (Acros organics)	0.007–0.06	
		33–75	humic acid (Leonardite)	0.043–0.09	
(Taketani et al., 2013)	296 ± 2	28–68	dicarboxylic acids include succinic, glutaric, adipic, and pimelic acid aerosol particles	0.02–0.18	lab
(Bedjanian et al., 2005)	240–350		soot	$(7.5 \pm 1.5) \times 10^{-2}$	lab
(Taketani et al., 2008)	296 ± 2	20–45; 45–75	$(NH_4)_2SO_4$	0.04–0.05 for dry aerosols; 0.11–0.19 for wet aerosols	lab
		20–53; 53–75	NaCl	<0.01–0.02 for dry aerosols; 0.09–0.11 for wet aerosols	lab
(Lakey et al., 2016)	293 ± 2	60 ± 3	Copper-doped ammonium sulfate aerosols with the addition of different organic species at organic to copper molar ratio of 2:1 or 10:1	0.003–0.23	lab
(Taketani et al., 2012)	298	75	Regenerated aerosol particles sampled from ambient air at Mts. Tai and Mang in China	0.09–0.40	field
(Zhou et al., 2020)	ambient	ambient	Ambient aerosols in Kyoto, Japan during the summer of 2018	0.08–0.36	field

Table S2. Summary of F0AM inputs for base and two perturbation simulations derived from various GEOS-Chem simulations.

	GEOS-Chem output variables used as inputs to F0AM	F0AM-base	F0AM-no_rad	F0AM-no_chem
meteorology	Pressure, temperature, relative humidity	BASE	BASE	BASE
J-values	HONO, HCHO ($CO + 2HO_2$), HCHO ($H_2 + CO$)	BASE	NO_FIRE	BASE
Initial concentrations	Ethyne (C_2H_2), ethene (C_2H_4), propanal (C_2H_5CHO), butane (NC_4H_{10}), ethane (C_2H_6), propane (C_3H_8), ethanol (C_2H_5OH), hydroxyacetone (ACETOL), glycolaldehyde ($HOCH_2CHO$), glyoxal (GLYOX), formic acid (HCOOH), limonene (LIMONENE), methylglyoxal (MGLYOX), methacrolein (MACR), methyl vinyl ketone (MVK), acetaldehyde (CH_3CHO), formaldehyde (HCHO), methyl ethyl ketone (MEK), acetone (CH_3COCH_3), methanol (CH_3OH), alpha-pinene (APINENE), beta-pinene (BPINENE), isoprene (C_5H_8), propylene (C_3H_6), xylene (OXYL), toluene (TOLUENE), benzene (BENZENE), CO, O_3, OH, HO_2, H_2O_2, NO, NO_2, PAN, HNO_3, N_2O_5, HONO	BASE	BASE_NO_RAD	BASE_NO_CHEM
Aerosols	Surface areas and radii for OC, BC, SULF, SSA, SSC, MDUST (7 size bins)	BASE	BASE	NO_FIRE
Background concentrations	NO, NO_2, PAN, HONO, HNO_3, O_3, OH, HO_2, H_2O_2, CO, HCHO, $HOCH_2CHO$	NO_FIRE	NO_FIRE	NO_FIRE
First-order dilution rate (k_{dil})	Calculated using CO decay and inversion of dilution equation: (Müller et al., 2016) $\frac{dX}{dt} = -k_{dil}(X(t) - X_{background})$			

*Note that our comparison includes only those fire plumes where aerosols are primarily contributed by smoke, specifically where more than 80% of the $PM_{2.5}$ mass is from smoke at a plume age of one hour. This selection criterion ensures that the differences between the BASE_NO_RAD (or BASE_NO_CHEM) and BASE simulations are primarily attributed to fire-related aerosols.

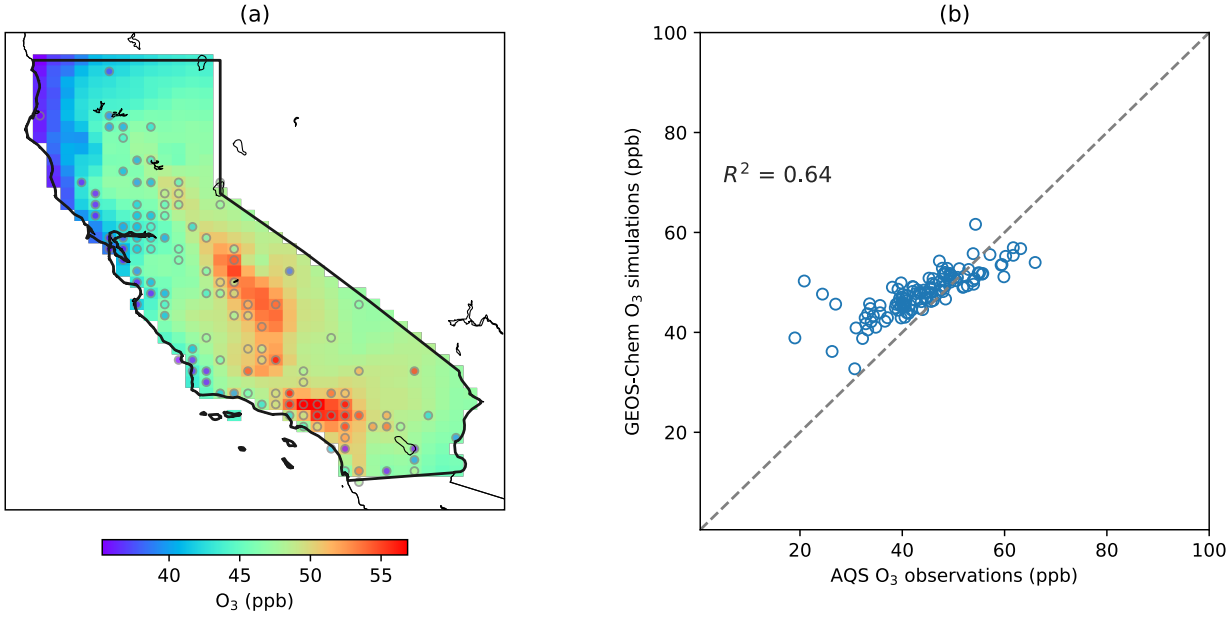

Figure S1. **(a)** Comparisons of 2020 GEOS-Chem simulations (γ_{HO_2} = 0.2) and EPA AQS ground measurements for O_3 around local 1 PM. The shaded areas represent GEOS-Chem simulations, and the dots indicate ground measurements. **(b)** Scatter plot of annual mean O_3 from GEOS-Chem simulations versus AQS observations.

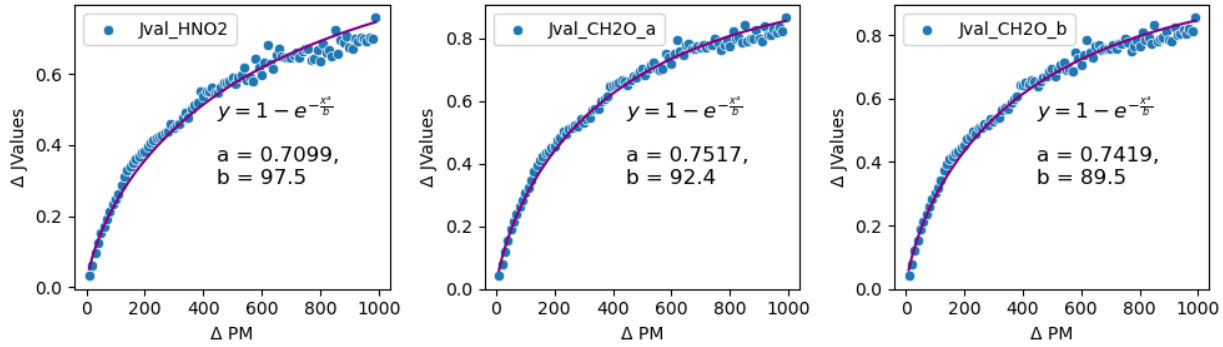

Figure S2. The relationship between the photolysis rate reduction (ΔJValues) for HONO, HCHO ($CO + 2HO_2$), HCHO ($H_2 + CO$) and $PM_{2.5}$ enhancement by fire ($\Delta PM_{2.5}$), derived from GEOS-Chem simulations over California region in September 2020. ΔJValues denote $\frac{JValues_{NO\_FIRE} - JValues_{BASE}}{JValues_{NO\_FIRE}}$, and $\Delta PM_{2.5}$ represents $PM_{2.5}$ mass concentrations between the BASE and NO_FIRE simulations (in units μg m^{-3}). The purple lines are exponential curves for fitting the relationship between PM enhancement and photolysis rate reduction.

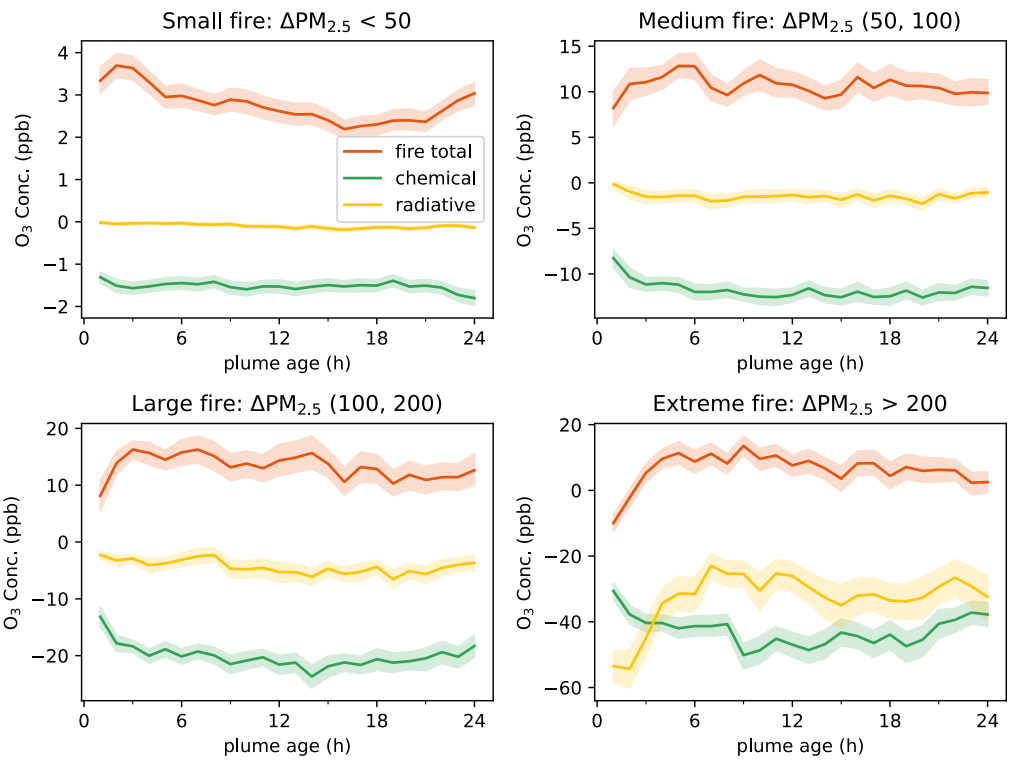

Figure S3. Aerosol effects on O_3 concentrations as a function of plume age for fire pixels grouped by size.

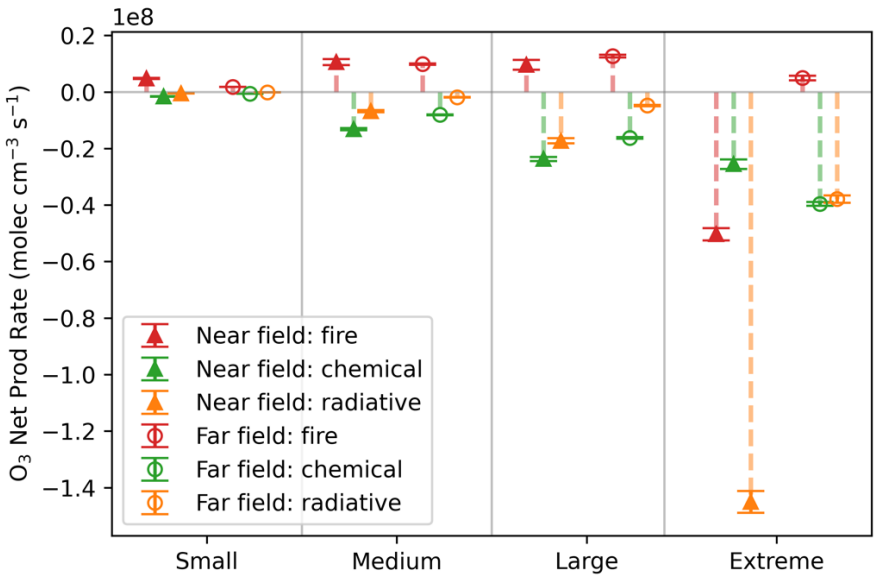

Figure S4. The overall fire impact and the two aerosol effects on O_3 net production rate at 20:30 UTC for all fire pixels in California during 2020, classified by PM enhancement and proximity to fire centers. The colors red, green and orange depict the total fire impact, aerosol chemical effect and radiative effect, respectively. Triangles and circles denote the near and far field, respectively, with error bars indicating standard errors.

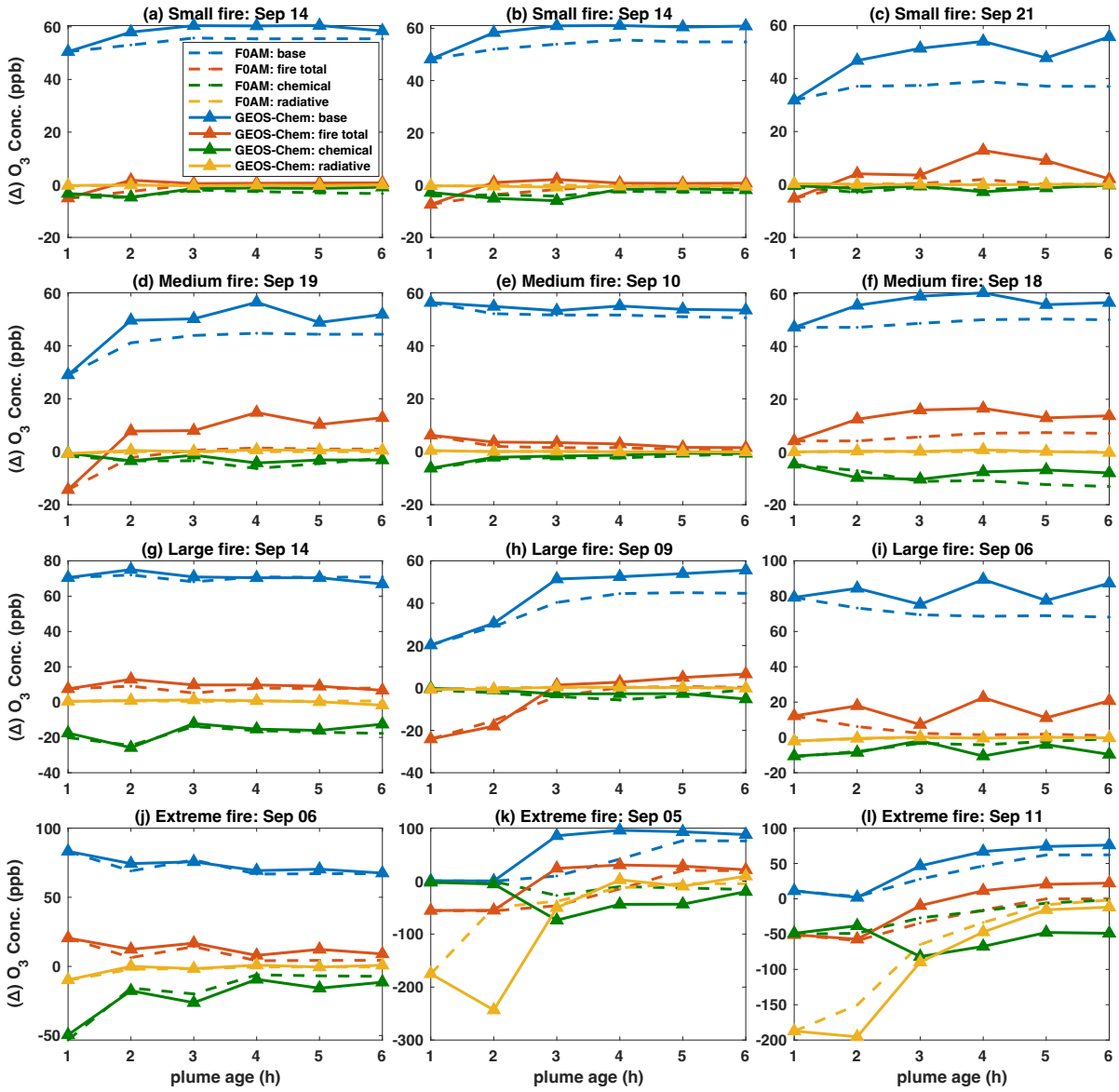

Figure S5. Comparison of aerosol effects on O_3 concentrations resolved in GEOS-Chem and in F0AM for fire plumes of different scales. $PM_{2.5}$ enhancement at plume age of one hour is used to approximately categorize fire sizes: <50 μg m^{-3}, 50–100 μg m^{-3}, 100–200 μg m^{-3} and >200 μg m^{-3} for small, medium, large and extreme fires, respectively. We include three plumes under each fire size category for comparison, each labeled by the date of the plume. O_3 simulations in F0AM are initiated with chemical concentrations, meteorological parameters and dilution factors derived from GEOS-Chem. The blue lines indicate O_3 concentrations from the base (with-fire) simulation, while the red, green and yellow lines represent changes in O_3 concentrations attributable to total fire effect, chemical effect and radiative effect, respectively. Solid lines represent GEOS-Chem simulations, and dashed lines denote F0AM outputs. To streamline the comparison between GEOS-Chem and F0AM amidst plume dispersions, we focus on the most probable trajectory, selecting a single GEOS-Chem grid box with the highest particle concentrations for each plume age.

(a)

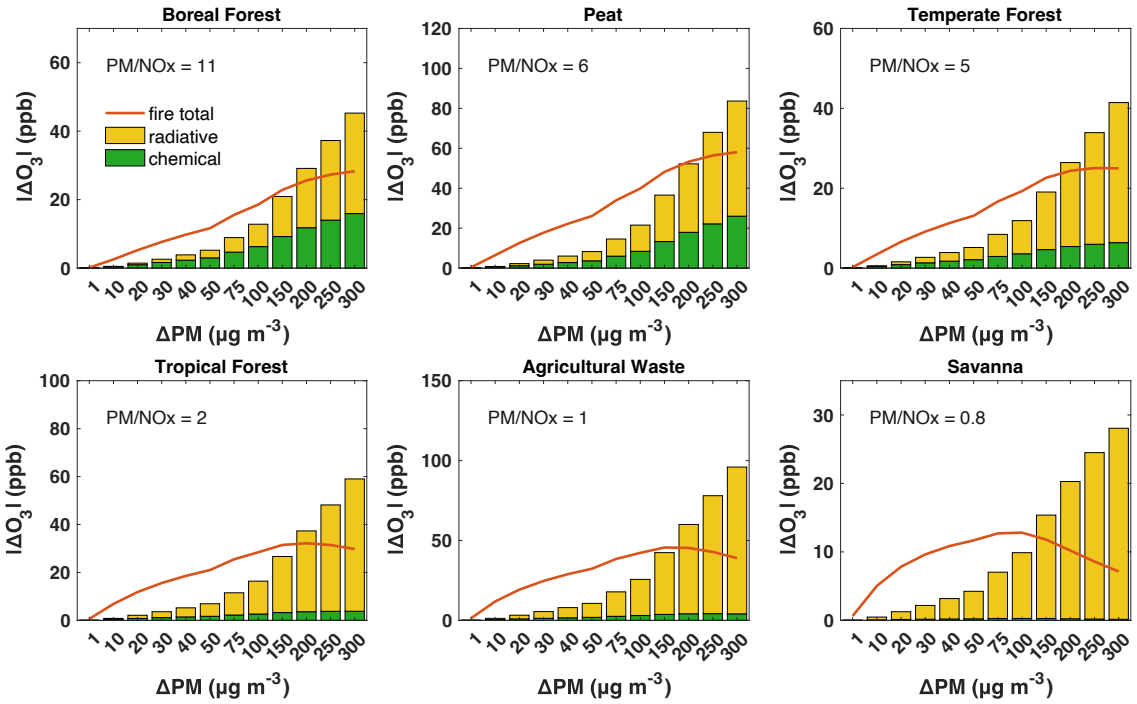

(b)

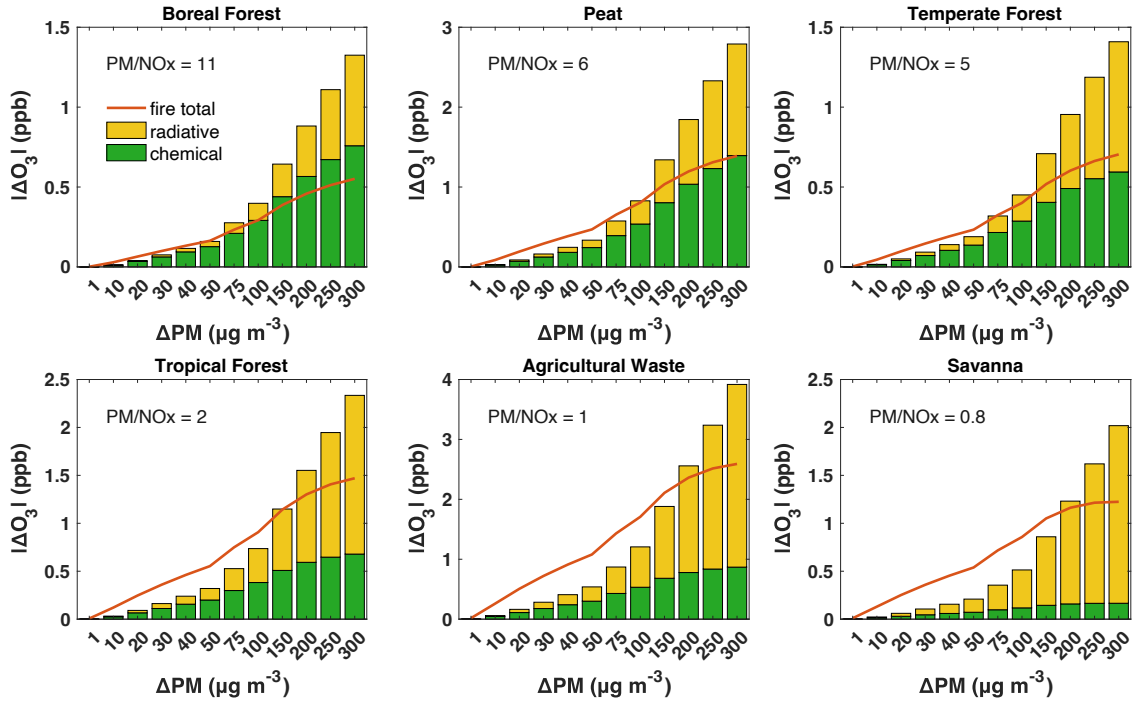

Figure S6. Sensitivity tests of aerosol effects across various fuel types in F0AM, with dilution rates increased by **(a)** 10× and **(b)** 100× relative to the original dilution rate of 1/86400~1×10^{-5} s^{-1}.

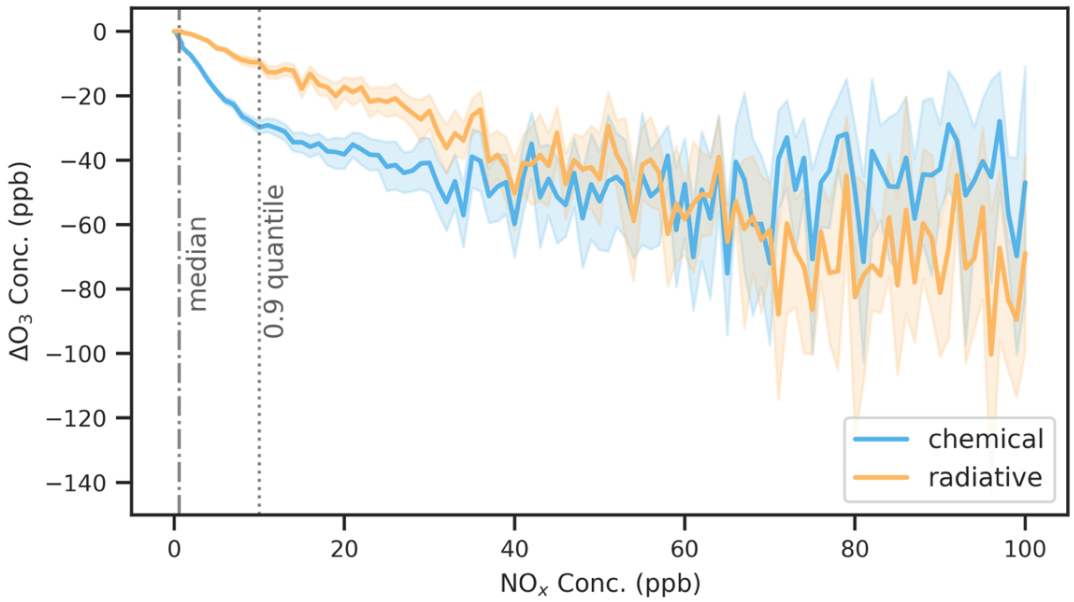

Figure S7. Dependence of aerosol chemical and radiative effects on NO_x concentrations at 20:30 UTC based on GEOS-Chem simulations. The analysis includes all fire pixels within identified plumes.

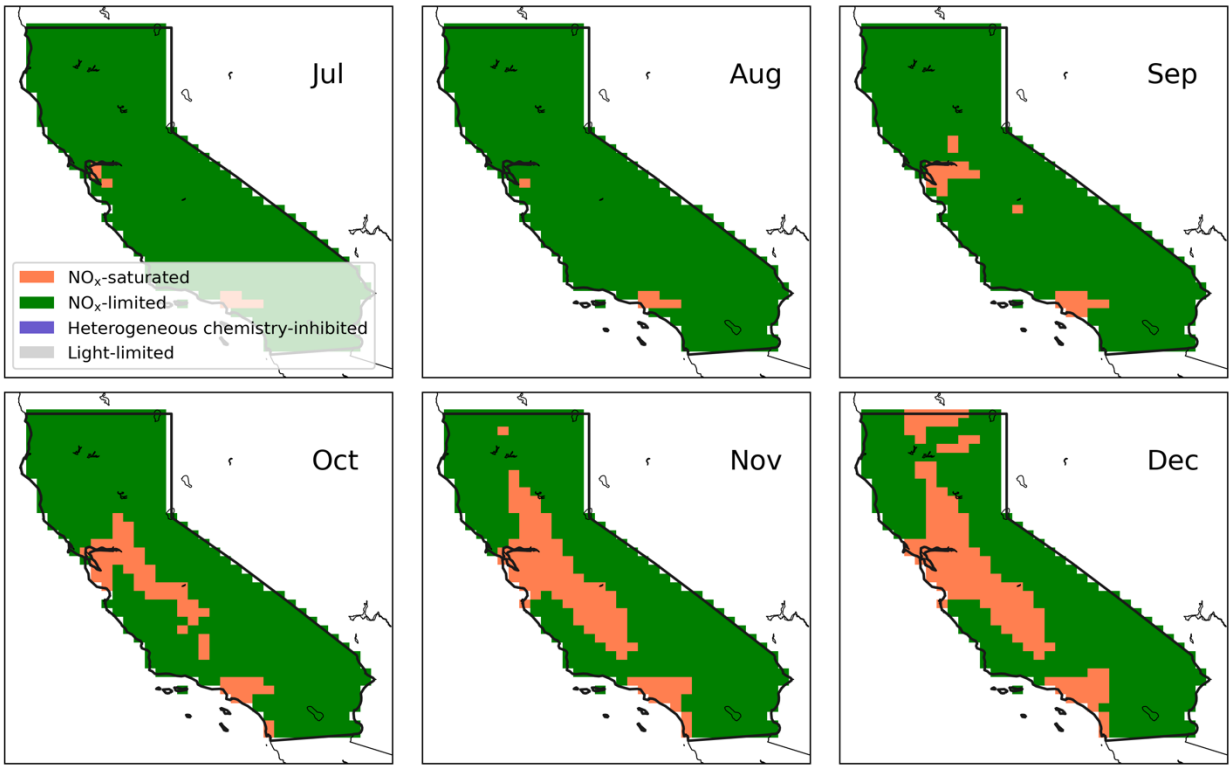

Figure S8. Monthly-mean O_3 photochemical regimes at 20:30 UTC over California, from July to December 2020 under the NO_FIRE scenario.

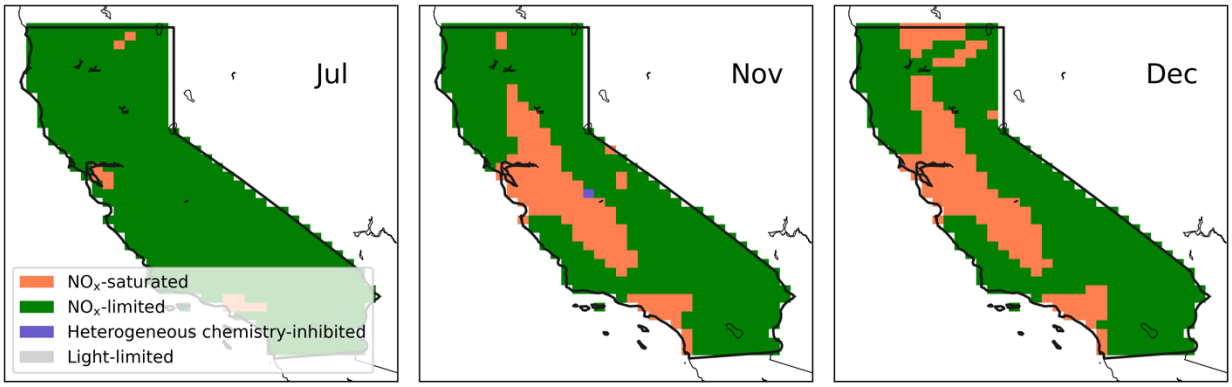

Figure S9. Monthly-mean O_3 photochemical regimes at 20:30 UTC over California, for July, November and December, when fires are accounted.

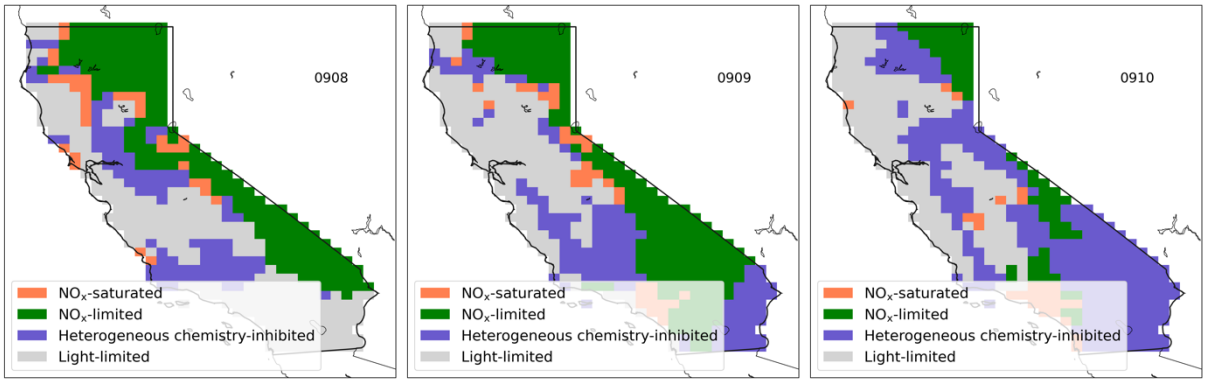

Figure S10. Daily O_3 photochemical regimes at 20:30 UTC over California under the BASE scenario (γ_{HO_2}= 0.2), from September 8–10.

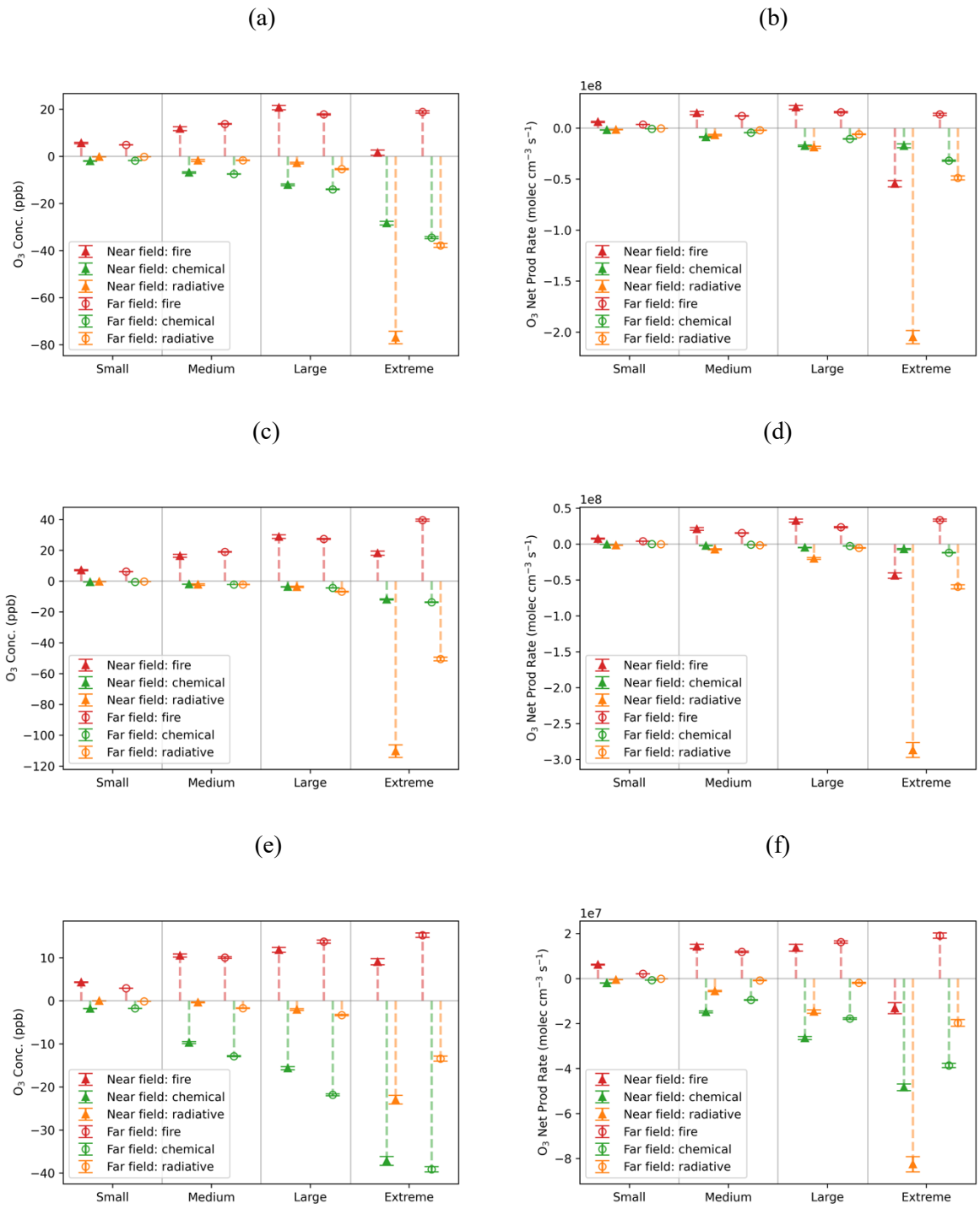

Figure S11. Sensitivity tests of total fire effects and aerosol effects on O_3 concentrations **(a, c, e)** and O_3 net production rate **(b, d, f)** at 20:30 UTC for fire pixels of different sizes in both near and far field. Panels **(a) and (b)** use γ_{HO_2} of 0.1 and include all 470 plumes from September 2020. Panels **(c) and (d)** use a lower γ_{HO_2} value of 0.02, based on all September plumes. Panels **(e) and (f)** are based on adjusted GFED emissions and include 1347 plumes identified between July and December 2020.

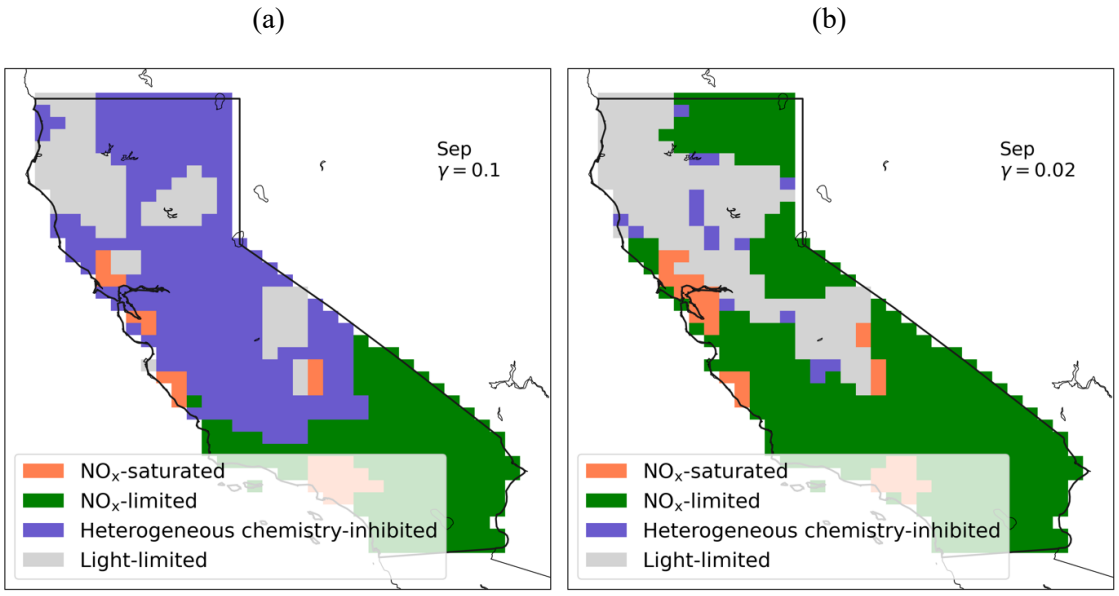

Figure S12. Monthly-mean O_3 photochemical regimes at 20:30 UTC over California for September 2020, under the BASE scenario with **(a)** γ_{HO_2}= 0.1 and **(b)** γ_{HO_2}= 0.02.

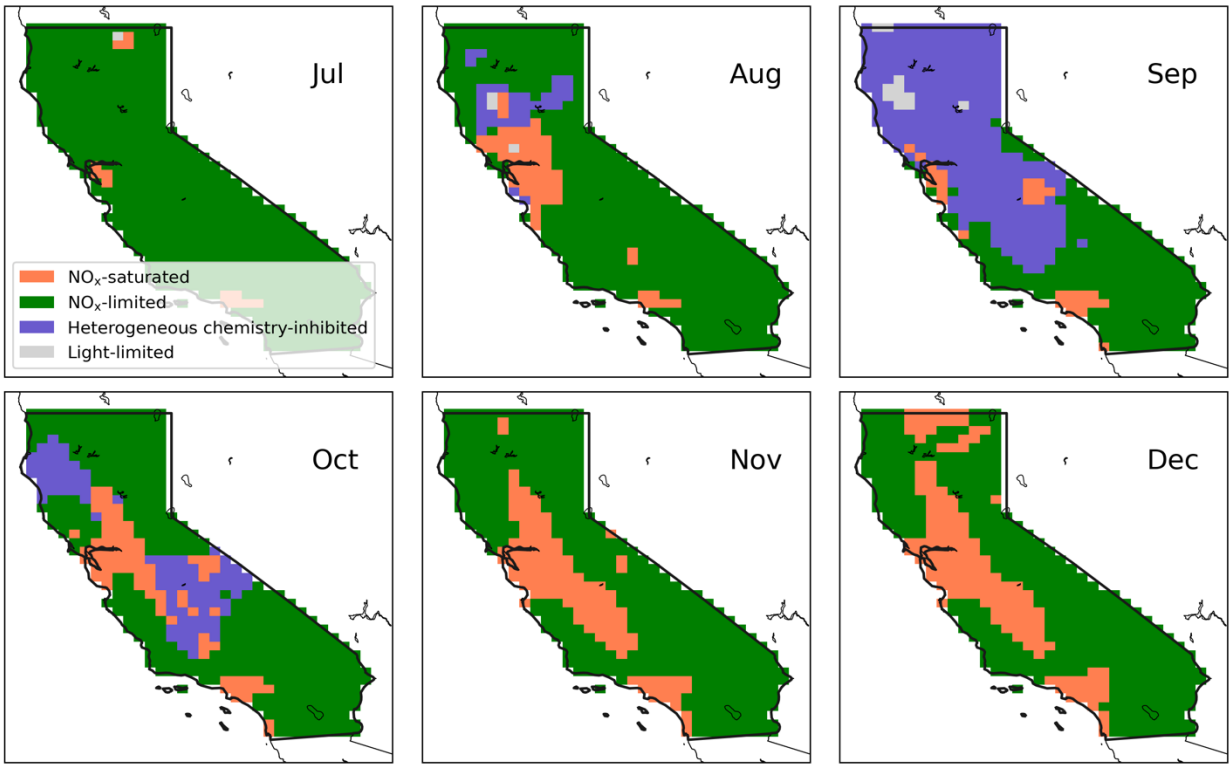

Figure S13. Monthly-mean O_3 photochemical regimes at 20:30 UTC over California, from July to December 2020 under the BASE scenario (γ_{HO_2}= 0.2), but with biomass burning emissions adjusted for each month based on GEOS-Chem simulations vs. ground observations. The ratios of GEOS-Chem to EPA AQS $PM_{2.5}$ measurements from July to December (approximately 0.6, 1.2, 4.1, 2.4, 1.4 and 0.9) are used to scale the monthly biomass burning emissions in GEOS-Chem.

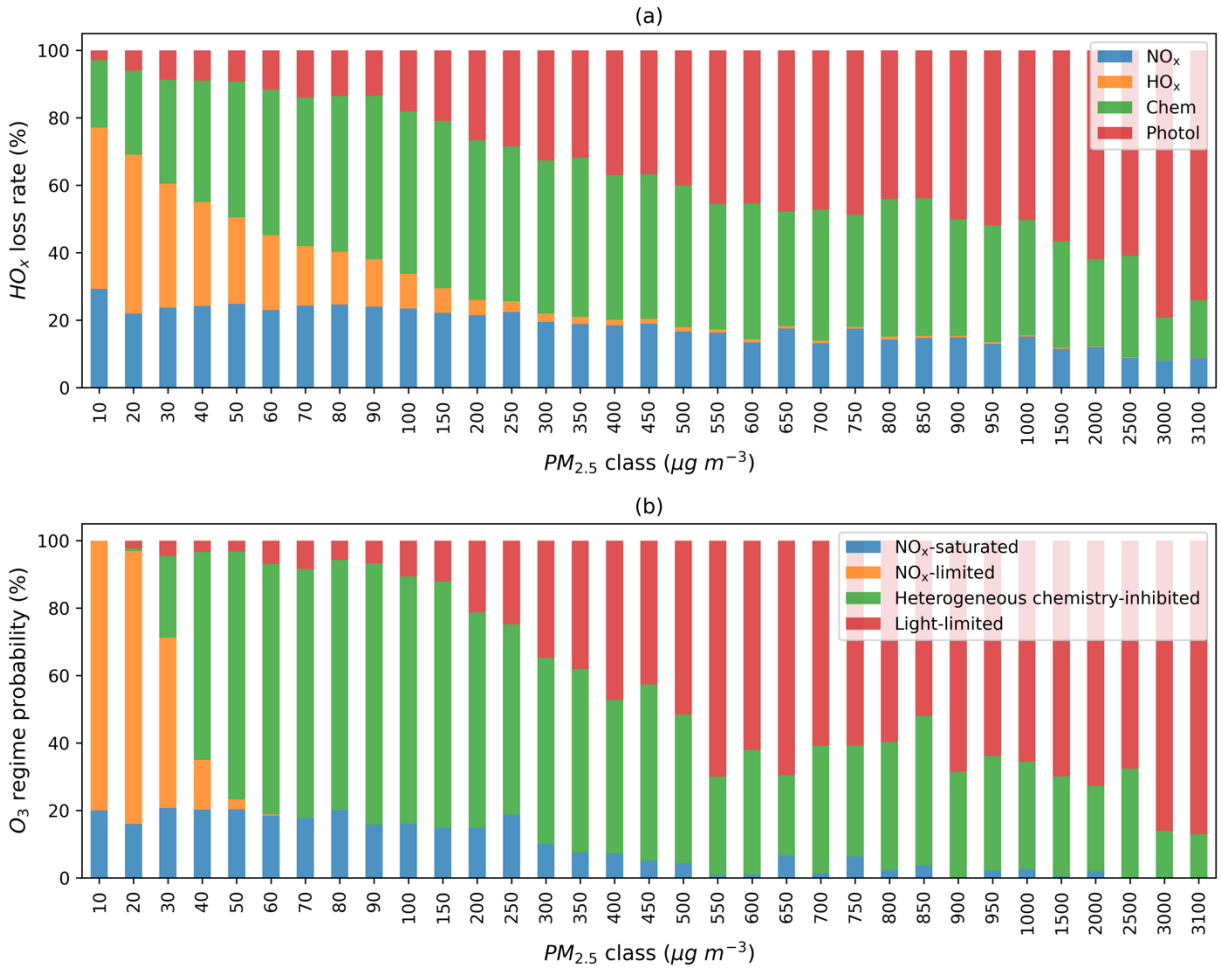

Figure S14. **(a)** the average fractional contribution of the four HO_x termination terms to the total; **(b)** the probability distribution of grid boxes across different regimes, at various $PM_{2.5}$ concentration levels, focusing exclusively on fire-affected grid boxes. Data are derived from hourly simulations at 20:30 UTC in California during September, with γ_{HO_2} = 0.1. Fire-affected grid boxes are selected based on $\Delta PM_{2.5}$ > 10 μg m^{-3}.

References

Bedjanian, Y., Lelièvre, S., and Bras, G. L.: Experimental study of the interaction of HO2 radicals with soot surface, Phys. Chem. Chem. Phys., 7, 334–341, https://doi.org/10.1039/B414217A, 2005.

CAL FIRE: California wildfires statistics, https://www.fire.ca.gov/our-impact/statistics, last access: 29 January 2025, 2020.

Carreras-Sospedra, M., Zhu, S., MacKinnon, M., Lassman, W., Mirocha, J. D., Barbato, M., and Dabdub, D.: Air quality and health impacts of the 2020 wildfires in California, Fire Ecology, 20, 6, https://doi.org/10.1186/s42408-023-00234-y, 2024.

Jin, X., Fiore, A. M., and Cohen, R. C.: Space-Based Observations of Ozone Precursors within California Wildfire Plumes and the Impacts on Ozone-NOx-VOC Chemistry, Environ. Sci. Technol., 57, 14648–14660, https://doi.org/10.1021/acs.est.3c04411, 2023.

Lakey, P. S. J., George, I. J., Whalley, L. K., Baeza-Romero, M. T., and Heard, D. E.: Measurements of the HO2 Uptake Coefficients onto Single Component Organic Aerosols, Environ. Sci. Technol., 49, 4878–4885, https://doi.org/10.1021/acs.est.5b00948, 2015.

Lakey, P. S. J., George, I. J., Baeza-Romero, M. T., Whalley, L. K., and Heard, D. E.: Organics Substantially Reduce HO2 Uptake onto Aerosols Containing Transition Metal ions, J. Phys. Chem. A, 120, 1421–1430, https://doi.org/10.1021/acs.jpca.5b06316, 2016.

Lassman, W., Mirocha, J. D., Arthur, R. S., Kochanski, A. K., Farguell Caus, A., Bagley, A. M., Carreras Sospedra, M., Dabdub, D., and Barbato, M.: Using Satellite-Derived Fire Arrival Times for Coupled Wildfire-Air Quality Simulations at Regional Scales of the 2020 California Wildfire Season, Journal of Geophysical Research: Atmospheres, 128, e2022JD037062, https://doi.org/10.1029/2022JD037062, 2023.

Müller, M., Anderson, B. E., Beyersdorf, A. J., Crawford, J. H., Diskin, G. S., Eichler, P., Fried, A., Keutsch, F. N., Mikoviny, T., Thornhill, K. L., Walega, J. G., Weinheimer, A. J., Yang, M., Yokelson, R. J., and Wisthaler, A.: In situ measurements and modeling of reactive trace gases in a small biomass burning plume, Atmospheric Chemistry and Physics, 16, 3813–3824, https://doi.org/10.5194/acp-16-3813-2016, 2016.

Safford, H. D., Paulson, A. K., Steel, Z. L., Young, D. J. N., and Wayman, R. B.: The 2020 California fire season: A year like no other, a return to the past or a harbinger of the future?, Global Ecology and Biogeography, 31, 2005–2025, https://doi.org/10.1111/geb.13498, 2022.

Taketani, F., Kanaya, Y., and Akimoto, H.: Kinetics of Heterogeneous Reactions of HO2 Radical at Ambient Concentration Levels with (NH4)2SO4 and NaCl Aerosol Particles, J. Phys. Chem. A, 112, 2370–2377, https://doi.org/10.1021/jp0769936, 2008.

Taketani, F., Kanaya, Y., and Akimoto, H.: Kinetics of HO2 Uptake in Levoglucosan and Polystyrene Latex Particles, J. Phys. Chem. Lett., 1, 1701–1704, https://doi.org/10.1021/jz100478s, 2010.

Taketani, F., Kanaya, Y., Pochanart, P., Liu, Y., Li, J., Okuzawa, K., Kawamura, K., Wang, Z., and Akimoto, H.: Measurement of overall uptake coefficients for HO_2 radicals by aerosol particles sampled from ambient air at Mts. Tai and Mang (China), Atmospheric Chemistry and Physics, 12, 11907–11916, https://doi.org/10.5194/acp-12-11907-2012, 2012.

Taketani, F., Kanaya, Y., and Akimoto, H.: Kinetic Studies of Heterogeneous Reaction of HO2 Radical by Dicarboxylic Acid Particles, International Journal of Chemical Kinetics, 45, 560–565, https://doi.org/10.1002/kin.20783, 2013.

Zhou, J., Murano, K., Kohno, N., Sakamoto, Y., and Kajii, Y.: Real-time quantification of the total HO2 reactivity of ambient air and HO2 uptake kinetics onto ambient aerosols in Kyoto (Japan), Atmospheric Environment, 223, 117189, https://doi.org/10.1016/j.atmosenv.2019.117189, 2020.